Programmable stopbands and supratransmission effects in a stacked Miura-origami metastructure

Qiwei Zhang,[1] Hongbin Fang,[2,3,4,*] and Jian Xu[2,3,4]

[1]*School of Aerospace Engineering and Applied Mechanics, Tongji University, Shanghai 200092, China*

[2]*Institute of AI and Robotics, Fudan University, Shanghai 200433, China*

[3]*Engineering Research Center of AI & Robotics, Ministry of Education, Fudan University, Shanghai 20043, China*

[4]*Shanghai Engineering Research Center of AI & Robotics, Fudan University, Shanghai 200433, China*

(Received 8 January 2020; accepted 23 March 2020; published 13 April 2020)

Origami-based mechanical metamaterials and metastructure have been demonstrated to exhibit unique properties originating from their intricate geometries of folding. This research aims to extend the current investigation level from quasistatics to dynamics. In detail, this research focuses on the wave dynamics of a metastructure composed of stacked Miura-origami (SMO) units. The SMO unit could possess two stable configurations, endowing the metastructure with rich possibilities in the layout of its periodic repeating cell. Through linear dispersion analyses and numerical studies, we show that the long-desired stopband tunability and programmability of the metastructure along the three principal directions can be acquired by strategically programming the layout of the periodic cell. Based upon that, we further discover that energy supratransmission through the metastructure is possible within the stopband by increasing the driving amplitude. Through numerical means, the amplitude threshold of supratransmission is obtained. We demonstrate that the fundamental mechanism that triggers the supratransmission phenomenon is the transition of the responses from the low-energy intrawell oscillations to the high-energy interwell oscillations. Numerical studies also indicate that the supratransmission threshold can be effectively tailored by adjusting the periodic cell layout. The results of this research provide a wealth of fundamental insights into the origami wave dynamics and offer useful guidelines for developing origami metastructures with tunable and programmable dynamic characteristics.

DOI: 10.1103/PhysRevE.101.042206

I. INTRODUCTION

Recently, there are growing appeals for origami structures. As an ancient art of paper folding, origami has been widely used in many research fields such as bionics, architecture, mathematics, material science, and robotics. For example, inspired by the exquisite folding pattern of the earwig wing, a spring origami model was developed for achieving tunable and programmable morphing functionalities [1]. Actuated by an external Hall effect sensor array, a miniature magnetic origami robot has been designed and prototyped for potential *in vivo* applications [2]. The above ingenious engineering structures all benefit from the infinite and rich geometries of origami. In fact, complex three-dimensional (3D) shapes can be obtained by folding two-dimensional (2D) flat sheets based on meticulously designed crease patterns. In addition to constructing delicate 3D structures, another useful aspect of origami is that folding could induce attractive and even unorthodox mechanical properties that are missing in conventional materials and structures. For example, origami-based mechanical metamaterials and metastructures [3] have been demonstrated to exhibit negative Poisson's ratios [4], structural multistability [5–7], programmable stiffness [8–11], self-locking [12], mechanical diode effect [13], and recoverable collapse [14], etc.

Although substantial progress has been achieved in the mechanics of origami, previous studies mainly focused on the static or quasistatic characteristics, and the dynamic folding/unfolding behavior of origami has been relatively unexplored Note that in practice, origami-based structures will inevitably work in dynamic environment. For example, origami devices may suffer from external excitations, and origami metamaterials and metastructures may serve as media for wave propagation. Therefore, extending the origami study from statics to dynamics is a natural next step. Roughly speaking, the limited current studies on origami dynamics can be divided into two categories, namely, vibration dynamics and wave dynamics. In terms of vibration dynamics, Fang *et al.* conducted a comprehensive investigation on the rich dynamics of a bistable stacked Miura-origami (SMO) structure. It has been demonstrated theoretically and experimentally that the intrinsic bistability could induce complex dynamical behaviors, including regular periodic oscillations, subharmonic oscillations, and chaotic oscillations [15]. In terms of wave dynamics, Yasuda *et al.* investigated the nonlinear wave propagation in origami-based metamaterials consisting of Tachi-Miura polyhedron (TMP) cells [16] and triangulated cylindrical origami (TCO) cells [17]. They found that the TMP-based and the TCO-based metamaterials can be highly useful for mitigating impacts by converting compressive waves into rarefaction waves. In another study, Thota *et al.* developed an origami-based metastructure for tuning phononic bandgap via folding [18,19]; this design concept has also been

*fanghongbin@fudan.edu.cn

employed for developing a reconfigurable origami traffic noise barrier [20].

Note that although there is a lack of research on origami wave dynamics, considerable efforts have been devoted to the wave propagation in conventional nonlinear and multistable metastructures, especially in terms of their bandgaps and nonlinear supratransmission effects. For elastic waves, bandgaps are defined as the frequency range in which wave transmission is prohibited in the investigated periodic structure [21]. Such phenomena can be utilized in designing acoustic filters, noise silencers, and vibration shields [22]. Generally, metamaterials and metastructures rely on structural periodicity to induce Bragg scattering effects [23] and to create bandgaps at certain frequency ranges [24,25]. Providing that the oscillation amplitude is small, most research on band structures are based on linear dispersion analysis. In detail, by linearizing the system about its stable state and assuming solutions in the form of a traveling wave, the model can be reduced into a standard eigenvalue problem, and the band structure can be determined by sweeping the wave number. Several methods have been developed to calculate the bandgaps of periodical structures, such as the transfer matrix method [26–28], the finite different time-domain method [29,30], the multiscattering theory [31], and the finite element method [21,32]. However, when the driving frequency locates within the stopband of the nonlinear periodic structure, there exists a threshold of the driving amplitude, beyond which a sudden increase in the energy penetration through the medium happens due to the intrinsic nonlinear process. Such a phenomenon was first observed by Geniet and Leon and was named as nonlinear supratransmission [33]. Due to its potential applications in energy transmission and waveguide, considerable research efforts have been devoted to the analysis of supratransmission in different physical systems, such as the Fermi Pasta Ulam chain [34], the sine-Gordon and Klein-Gordon chains [35,36], nonlinear waveguides [37,38], the discrete electrical lattices [39], etc. Determining the amplitude threshold is a key issue in analyzing the supratransmission phenomenon. Several kinds of indexes have been proposed to evaluate the threshold, including the energy flux [40], the injected energy [41], the total kinetic energy [34], and the velocity transmissibility [42]. To better understand the underlying mechanism and the sources, the supratransmission thresholds were also surveyed from the perspective of saddle-node bifurcation [37] and homoclinic orbit approach [38].

In the abovementioned studies, most metamaterials and metastructures are built upon either hypothetical elements (such as sine-Gordon and Klein-Gordon [33]) or conventional nonlinear oscillators (such as periodic bistable chain [41,43]). They can hardly be utilized for constructing practical structures. Evolution to a truly 3D system could serve as a better platform through which we would discover new characteristics of the band structure that have not been uncovered in previous studies. To fill this gap, we explore the utilization of origami, a fundamentally 3D structure with rich geometries and mechanical properties, such as the structural multistability and anisotropy. Specifically, in this paper, we focus on the stacked Miura-origami (SMO) structure, which has two stable configurations that are topologically different, namely, the nested-in and the bulged-out configurations [14]. The SMO structure is also a characteristic anisotropic 3D structure with distinctive constitutive relations along the three principal axes [44]. Moreover, serving as a constituent cell, the SMO structure can be tessellated along the three axes, and the elastic wave can also propagate along these three directions. The abovementioned features of the SMO structure, therefore, bring exciting opportunities to the research on the wave propagation in metamaterials and metastructures.

To advance the state of the art, the objectives of this research are twofold. First, based on the modularization concept and the linear wave propagation theory, we aim to explore the excellent bandgap tunability and programmability of the SMO metastructure in different wave propagation directions. Second, through in-depth numerical studies, we seek to unveil the supratransmission phenomena in origami metastructure and uncover its underlying mechanism that has never been reported. In doing so, this investigation could enhance our understanding of origami wave dynamics and provide useful design guidelines for creating real 3D engineering systems with the long-desired tunability and programmability of the wave propagation characteristics.

The rest of this paper is organized as follows. Section II reviews the fundamental geometry and quasistatic mechanics of the SMO structure. In Sec. III, the governing equations describing the nonlinear dynamics of the SMO metastructure is derived, followed by dispersion analysis based on the linearized system. In Sec. IV, we discuss the bandgap tunability and programmability of the metastructure originating from the structural bistability. We also demonstrate in this section that unlike conventional 1D lattices, the bandgaps of the origami metastructure can also be tuned and programmed in the other directions. In Sec. V, we move our focus to the supratransmission phenomenon when the driving amplitude is increased. The correlations between the threshold amplitude and the metastructure configuration are established, and the fundamental mechanism triggering the supratransmission is explored. Conclusions of this research and heuristic discussions are presented in Sec. VI.

II. GEOMETRY AND MECHANICS OF A STACKED MIURA-ORIGAMI UNIT

A stacked Miura-origami (SMO) unit consists of two Miura-origami sheets (sheet A and sheet B) [Fig. 1(a)]. The crease pattern of each sheet can be defined by the lengths of the two adjacent lines (a_k, b_k) and the sector angle between them (γ_k), where $k = \mathrm{A}, \mathrm{B}$, denoting sheet A and sheet B, respectively.

Under the rigid-folding assumption, the SMO unit retains a single degree-of-freedom (DoF) for folding. The folding motion can be characterized by the folding angle θ_A or θ_B defined as the dihedral angle between one of the Miura-origami facets and the reference x-o-y plane [Fig. 1(b)]. The parameters of the two Miura-origami sheets are not independent; rather, they have to satisfy the following compatibility conditions:

$$b_\mathrm{A} = b_\mathrm{B} = b,\ a_\mathrm{B}\cos\gamma_\mathrm{B} = a_\mathrm{A}\cos\gamma_\mathrm{A},$$
$$\cos\theta_\mathrm{B}\tan\gamma_\mathrm{B} = \cos\theta_\mathrm{A}\tan\gamma_\mathrm{A}. \quad (1)$$

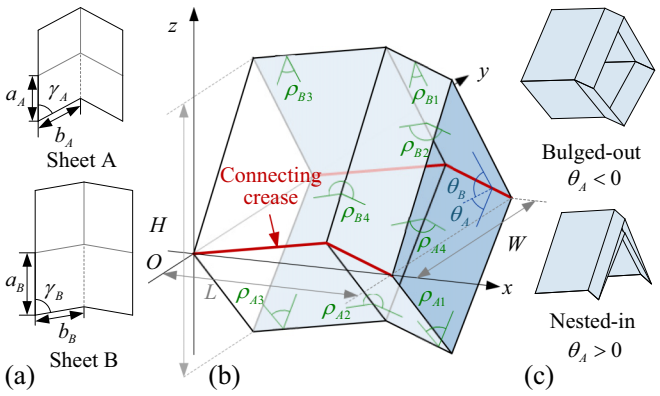

FIG. 1. (a) Geometry of the SMO unit. (a) The crease patterns of sheets A and B, the internal solid and dashed lines represent the "mountain" and "valley" creases, respectively. (b) 3D configuration of an SMO unit. (c) A single SMO structure at the bulged-out ($\theta_A < 0$)and the nested-in ($\theta_A > 0$) configurations.

Without loss of generality, θ_A is selected as the independent variable to describe the configuration of the SMO unit. Depending on whether $\theta_A \in (0, \pi/2)$ or $\theta_A \in (-\pi/2, 0)$, the SMO unit would exhibit two topologically different configurations, namely, nested-in and bulged-out configurations [Fig. 1(c)].

The external geometries (i.e., the length, the width, and the height) of the SMO unit can be described by

$$L = \frac{2b\cos\theta_A \tan\gamma_A}{\sqrt{1+\cos^2\theta_A \tan^2\gamma_A}}, W = 2a_A\sqrt{1-\sin^2\theta_A \sin^2\gamma_A},$$
$$H = a_B \sin\theta_B \sin\gamma_B - a_A \sin\theta_A \sin\gamma_A. \quad (2)$$

Folding of the SMO unit can also be described by the dihedral angles $\rho_{ki}(k = A, B; i = 1, ..., 4)$ between the adjacent facets [Fig. 1(b)], i.e.,

$$\rho_{k1} = \rho_{k3} = \pi - 2\theta_k, \rho_{k4} = 2\pi - \rho_{k2},$$
$$\rho_{k2} = 2\arcsin\left(\frac{\cos\theta_k}{\sqrt{1-\sin^2\theta_k \sin^2\gamma_k}}\right). \quad (3)$$

Particularly, for the nested-in configuration, we assign $\rho_{A2} \in (0, \pi)$, and for the bulged-out configuration, $\rho_{A2} \in (\pi, 2\pi)$. The dihedral angle at the connecting creases between sheet A and sheet B can be expressed as

$$\rho_C = \theta_B - \theta_A. \quad (4)$$

Under the rigid-folding assumption, the folding motion is considered as the rotation of the rigid facets with respect to the elastic hingelike creases. In this research, we assign k_A, k_B as the torsional stiffness per unit length for the creases in sheet A and sheet B, respectively, and k_C as the torsional stiffness per unit length for the connecting creases. Hence, the torsional stiffness constants corresponding to each crease can be determined. In sheet A, we have $K_{A1} = K_{A3} = k_A b$ and $K_{A2} = K_{A4} = k_A a_A$; in sheet B, we have $K_{B1} = K_{B3} = k_B b$, $K_{B2} = K_{B4} = k_B a_B$; for the connected lines, we have $K_C = k_C b$. Hence, the total potential energy of an SMO unit

TABLE I. Design parameters of the SMO unit.

Parameters	Values	Parameters	Values
$b_A = b_B = b$	26.7 mm	$k_A = k_C$	0.2 N/m
a_A	38.1 mm	k_B	1.4 N/m
a_B	43.4 mm	θ_A^0	-60°
γ_A	60°		

originating from the torsional stiffness at the creases yields

$$\Pi = \frac{1}{2}\left[\sum_{i=1}^{4} K_{Ai}\left(\rho_{Ai} - \rho_{Ai}^0\right)^2 + \sum_{i=1}^{4} K_{Bi}\left(\rho_{Bi} - \rho_{Bi}^0\right)^2 + 4K_C\left(\rho_C - \rho_C^0\right)^2\right], \quad (5)$$

where ρ_{Ai}^0, ρ_{Bi}^0, ρ_{Ci}^0 denote the dihedral angle when the SMO unit is at its stress-free configuration with $\theta_A = \theta_A^0$.

Fang *et al.* have found that the SMO unit would become bistable when the crease torsional stiffness of the sheet B creases (K_{Bi}) is sufficiently larger than sheet A creases (K_{Ai}) and connecting crease (K_C), or the stress-free folding angle (θ_A^0) far deviates away from 0° [15,44]. In this research, the design parameters of an SMO unit are listed in Table I, where the stiffness ratio $\mu = 7$ to ensure bistability. In what follows, unless otherwise noted, all studies are based on this design. Based on these parameters, Figs. 2(a)–2(c) displays the potential profiles of the SMO unit along the height, the length, and the width directions. It shows that with these parameters, the SMO unit is essentially bistable, with a nested-in and a bulged-out stable configurations.

Taking derivatives of the potential energy with respect to the H, L, and W:

$$F_H = \frac{d\Pi}{dH} = \frac{d\Pi}{d\theta_A}\left(\frac{dH}{d\theta_A}\right)^{-1},$$
$$F_L = \frac{d\Pi}{dL} = \frac{d\Pi}{d\theta_A}\left(\frac{dL}{d\theta_A}\right)^{-1},$$
$$F_W = \frac{d\Pi}{dW} = \frac{d\Pi}{d\theta_A}\left(\frac{dW}{d\theta_A}\right)^{-1}, \quad (6)$$

the force-displacement relations along the height, the length, and the width directions can be obtained [Figs. 2(d)–2(f)]. It reveals that the constitutive relations along the three principal directions are qualitatively different. We will discuss in Sec. IV that such distinct constitutive relations would trigger different wave propagation characteristics.

III. MODELING OF THE SMO METASTRUCTURE

Figure 3 displays schematic designs of the SMO metastructures, which consists of 61 SMO units. Since the SMO unit is a true 3D structure, the metastructure can be obtained by tessellating the constituent units in series along the length (L), the width (W), or the height (H) directions, showing in Figs. 3(a)–3(c), respectively. Here, connections between adjacent cells are achieved by rigid rods, such that folding of the constituent units remain independent. In what follows, the modeling will be exemplified by the

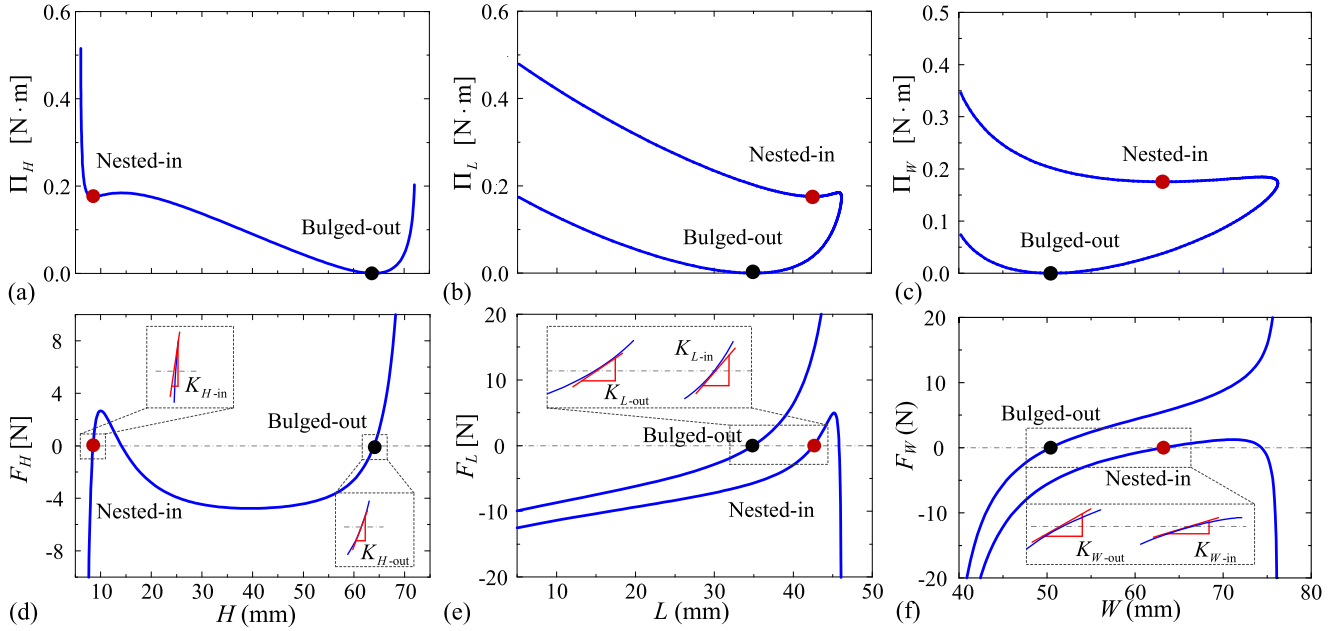

FIG. 2. The energy landscapes (a), (b), and (c) and the force-displacement curves (d), (f), and (e) of the SMO unit along different orientations. The solid circles denote the stable bulged-out and nested-in configurations.

scenario that the metastructure is connected along the height direction.

To simplify the modeling, we equivalently represent the mass of the SMO unit into a lumped mass m and the force-displacement relation into a nonlinear spring such that each SMO unit along the height direction can be described as a nonlinear lumped-mass oscillator. Considering that the tangent stiffness around the stable nested-in and the stable bulged-out configurations could be significantly different, we use two different nonlinear oscillators to represent them, denoted by the orange and blue circles, respectively. To precisely tackle the nonlinear force-displacement relation and to ensure computational efficiency, we use a 15th-order polynomials to approximate the force-displacement curve. Specifically, we use $F_{\text{in}}(s)$ and $F_{\text{out}}(s)$ to represent the constitutive relation corresponding to the nested-in and the bulged-out configurations, respectively, where s denotes the deformation of the unit measuring from the corresponding stable

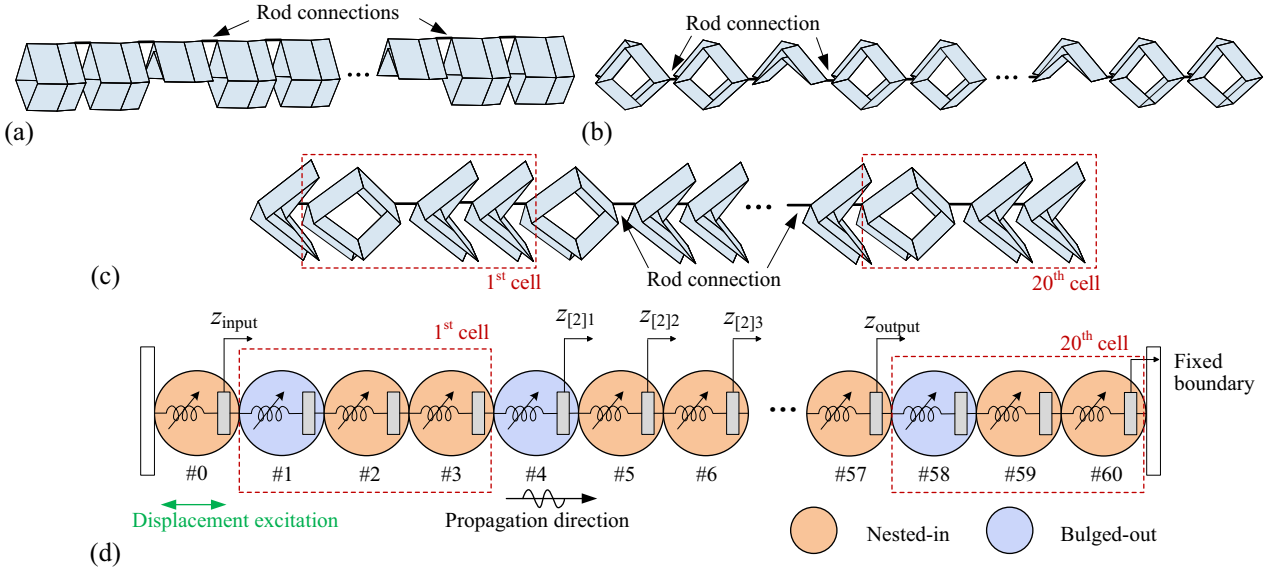

FIG. 3. Conceptual designs and the equivalent model of the SMO metastructure. The metastructures are constructed by connecting SMO units in series along (a) the length direction, (b) the width direction, and (c) the height direction via rigid rods. (d) A schematic nonlinear oscillator representation of the metastructure given in (c). A single SMO unit is equivalently modeled as a lumped mass with a nonlinear spring. The nested-in and the bulged-out configuration of the constituent SMO units are represented by orange circles and blue circles, respectively. A periodic repeating cell is highlighted with a red dashed box.

configuration.

$$F_{\text{in}}(s) = \alpha_1 s + \alpha_2 s^2 + \ldots \alpha_{15} s^{15},$$
$$F_{\text{out}}(s) = \beta_1 s + \beta_2 s^2 + \ldots \beta_{15} s^{15}. \tag{7a}$$

$$s = H - H_{\text{in}} \quad \text{for} \quad F_{\text{in}},$$
$$s = H - H_{\text{out}} \quad \text{for} \quad F_{\text{out}}. \tag{7b}$$

Based on the above simplification, the metastructure can then be described as a chain of nonlinear oscillators [Fig. 3(d)], where all masses are equal, and only the nearest neighbors have direct effects on each other. The actuation is applied on the left side of the chain, which can be modeled as a displacement input z_{in} applied to the mass of the first oscillator (#0) next to the left boundary. On the right side of the chain, the last oscillator (#60) connects with a fixed boundary by a nonlinear spring $F_{\text{in}}(s)$ to ensure periodicity. The output signal z_{out} is measured from one cell away from the boundary, i.e., the mass in the #57 oscillator.

Assuming that a periodic cell consists of three SMO units showing in Fig. 3(d), equations of motion (EOM) for the pth cell can be expressed as

$$m\ddot{z}_{[p]1} + F_{\text{out}}(z_{[p]1} - z_{[p-1]3}) - F_{\text{in}}(z_{[p]2} - z_{[p]1}) = 0, \tag{8a}$$

$$m\ddot{z}_{[p]2} + F_{\text{in}}(z_{[p]2} - z_{[p]1}) - F_{\text{out}}(z_{[p]3} - z_{[p]2}) = 0, \tag{8b}$$

$$m\ddot{z}_{[p]3} + F_{\text{in}}(z_{[p]3} - z_{[p]2}) - F_{\text{out}}(z_{[p+1]1} - z_{[p]3}) = 0. \tag{8c}$$

Equation (8a) is valid to $\forall p \in [2, 20]$, Eq. (8b) is valid to $\forall p \in [1, 20]$, and Eq. (8c) is valid to $\forall p \in [1, 19]$. The EOM for the first and last oscillator in the metastructure can be modified as

$$m\ddot{z}_{[1]1} + F_{\text{out}}(z_{[1]1} - z_{\text{input}}) - F_{\text{in}}(z_{[1]2} - z_{[1]1}) = 0, \tag{9a}$$

$$m\ddot{z}_{[20]3} + F_{\text{in}}(z_{[20]3} - z_{[20]2}) - F_{\text{in}}(0 - z_{[20]3}) = 0. \tag{9b}$$

In the above equations, $z_{[p]q}$ denotes the global displacement of the mass in the p-th oscillator of the qth cell ($p = 1, ..., 20$) and $q = 1, 2, 3$ in this example. The initial positions of the lumped masses locate at the stable nested-in or bulged-out configurations.

Considering small amplitudes of the displacement input, the following transformation is introduced:

$$z_{[p]q} = \varepsilon \tilde{z}_{[p]q} (p = 1, ..., 20; q = 1, 2, 3). \tag{10}$$

Hence, $z_{[p]q}$ becomes of order $O(\varepsilon)$ and $\tilde{z}_{[p]q}$ becomes of order $O(1)$. Substituting Eqs. (7) and (10) into Eqs. (8) and (9), and neglecting the high-order terms of ε, the EOM yields

$$m\ddot{\tilde{z}}_{[p]1} + k_{\text{out}}(\tilde{z}_{[p]1} - \tilde{z}_{[p-1]3}) - k_{\text{in}}(\tilde{z}_{[p]2} - \tilde{z}_{[p]1}) = 0, \tag{11a}$$

$$m\ddot{\tilde{z}}_{[p]2} + F_{\text{in}}(\tilde{z}_{[p]2} - \tilde{z}_{[p]1}) - F_{\text{out}}(\tilde{z}_{[p]3} - \tilde{z}_{[p]2}) = 0, \tag{11b}$$

$$m\ddot{\tilde{z}}_{[p]2} + F_{\text{in}}(\tilde{z}_{[p]2} - \tilde{z}_{[p]1}) - F_{\text{out}}(\tilde{z}_{[p]3} - \tilde{z}_{[p]2}) = 0, \tag{11c}$$

and

$$m\ddot{\tilde{z}}_{[1]1} + F_{\text{out}}(\tilde{z}_{[1]1} - \tilde{z}_{\text{input}}) - F_{\text{in}}(\tilde{z}_{[1]2} - \tilde{z}_{[1]1}) = 0, \tag{12a}$$

$$m\ddot{\tilde{z}}_{[20]3} + F_{\text{in}}(\tilde{z}_{[20]3} - \tilde{z}_{[20]2}) - F_{\text{in}}(0 - \tilde{z}_{[20]3}) = 0, \tag{12b}$$

where $k_{\text{in}} = \alpha_1$ and $k_{\text{out}} = \beta_1$, denoting the corresponding linearized stiffness of the origami cell at the nested-in and the bulged-out configurations, respectively.

Assuming that the solution of Eq. (11) in the form of a traveling wave, i.e.,

$$\tilde{z}_{[p]1} = \text{A}e^{i(\omega t - kpL)},$$
$$\tilde{z}_{[p]2} = \text{B}e^{i[\omega t - k(p+1)L]}, \tag{13}$$
$$\tilde{z}_{[p]3} = \text{C}e^{i[\omega t - k(p+2)L]},$$

where k is the wave number and $L = 1$ is the unit length. Hence, the model can be reduced to a standard eigenvalue problem

$$\begin{pmatrix} k_{\text{out}} + k_{\text{in}} & -k_{\text{in}}e^{i(-kL)} & -k_{\text{out}}e^{i(-kL)} \\ -k_{\text{in}}e^{i(kL)} & k_{\text{in}} + k_{\text{in}} & -k_{\text{in}}e^{i(-kL)} \\ -k_{\text{out}}e^{i(kL)} & -k_{\text{in}}e^{i(kL)} & k_{\text{in}} + k_{\text{out}} \end{pmatrix} \begin{pmatrix} \text{A} \\ \text{B} \\ \text{C} \end{pmatrix} = m\omega^2 \begin{pmatrix} \text{A} \\ \text{B} \\ \text{C} \end{pmatrix}. \tag{14}$$

The stopbands and passbands of the metastructure can then be determined by sweeping the wave number k from 0 to π. If with different periodic repeating cells, then the corresponding band structures can be determined based on similar linear dispersion analysis.

To demonstrate the introduced method above, without loss of generality, we consider four cases that the periodic repeating cell consists of three SMO units remaining at different stable configurations. Specifically, if denoting the nested-in and the bulged-out configuration by binary numbers "0" and "1," the four cases can be expressed as the state sequence of the constituent SMO units in a cell, namely, (1A) "0-0-0," (1B) "1-1-1," (3A) "1-0-0," and (3B) "0-1-1." With the lumped mass $m = 0.12$kg and the other parameters given in Table I, the band structures corresponding to the four cases can be theoretically obtained by solving Eq. (14), showing in the left panels of the subfigures in Fig. 4. For the first two cases, the periodic cell consists of identical SMO units [Figs. 4(a) and 4(b)]. However, the band structures exhibit obvious differences. For case (1A), the only stopband locates within [65.00, ∞) Hz; while for case (1B), the stopband is significantly broadened to [29.79, ∞) Hz. In the left two cases, the periodic cell consists of different SMO units [Figs. 4(c) and 4(d)]. Surprisingly, the band structures are dramatically altered in both the number and the locations. For case (3A), there are three stopbands locating within [16.77, 32.50] Hz, [38.79, 56.29] Hz, and [57.72, ∞) Hz; for case (3B), the stopbands shift to [14.89, 19.82] Hz, [25.79, 48.32] Hz, and [48.83, ∞) Hz.

To verify the correctness of the theoretical results, numerical frequency sweeps are also performed on the metastructure based on Eqs. (8) and (9). Specifically, harmonic displacement excitation with amplitude 0.01mm is applied to the most left mass of the chain. The excitation frequency is swept from 0.1 to 75 Hz, with step 0.1 Hz. The output signal is measured from one cell away from the right boundary, i.e., the mass in the #57 oscillator. Small viscous damping with coefficient $\zeta = 0.001$ is assumed between adjacent SMO units. At each excitation frequency, zero initial displacement and velocity are set. In this research, we use the root mean square (RMS) value of the displacement data to characterize the

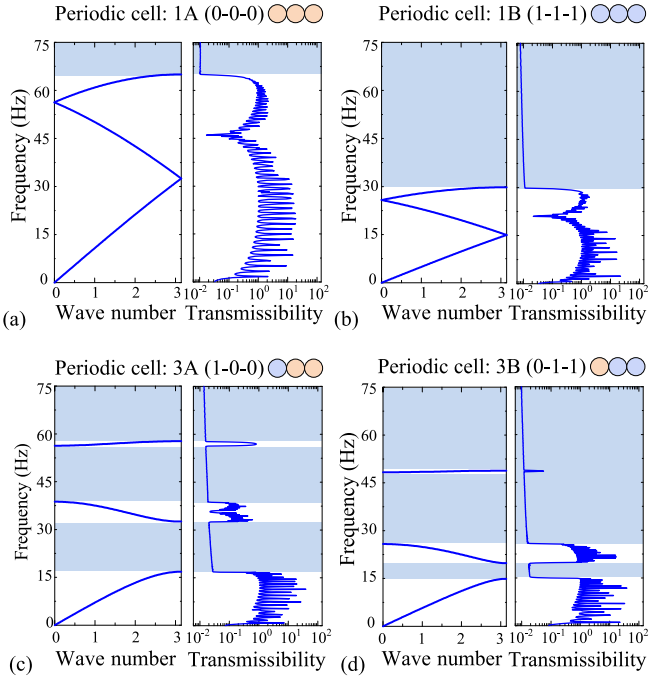

FIG. 4. Band structure and transmissibility of the SMO metastructure based on different periodic cells. (a) Periodic cell 1A (0-0-0); (b) periodic cell 1B (1-1-1); (c) periodic cell 3A (1-0-0); and (d) periodic cell 3B (0-1-1). The left panels show the bandgaps obtained via linear dispersion analysis, and the right panels display the numerically obtained frequency-transmissibility relations.

average vibration energy. Hence, by dividing the RMS of the output displacement (z_{output}) by the RMS of the input displacement (z_{input}), we derive the displacement transmissibility $T = |\text{RMS}(z_{\text{output}})|/|\text{RMS}(z_{\text{input}})|$. In Fig. 4, the numerically obtained frequency-transmissibility diagrams are displayed in the right panels of subfigures. If defining the stopband as the frequency interval in which the transmissibility is lower than 0.1, we notice that the numerically determined stopbands agree perfectly with those determined via linear dispersion analysis.

Overall, Fig. 4 suggests that the band structure, including the number and the locations of the stopbands, can be effectively tailored by switching the configuration of the constituent bistable SMO unit (between the "0" and "1" configurations) in the periodic repeating cell. Considering that the number of the SMO units in the periodic cell can also be tuned, programmability of the stopband within a broad frequency range can be further expected. Moreover, since the SMO unit is a true 3D shape, the bandgap of the metastructure along the other two directions can be determined via a similar linear dispersion analysis. It is also worth expanding the bandgap tunability and programmability study to all the three principal directions.

IV. BANDGAP TUNABILITY AND PROGRAMMABILITY

A. Rich possibilities of the periodic repeating cell

Before discussing the tunability and programmability, we first study the possibilities for constructing the periodic repeating cell. Here, as examples, we consider the cases that the

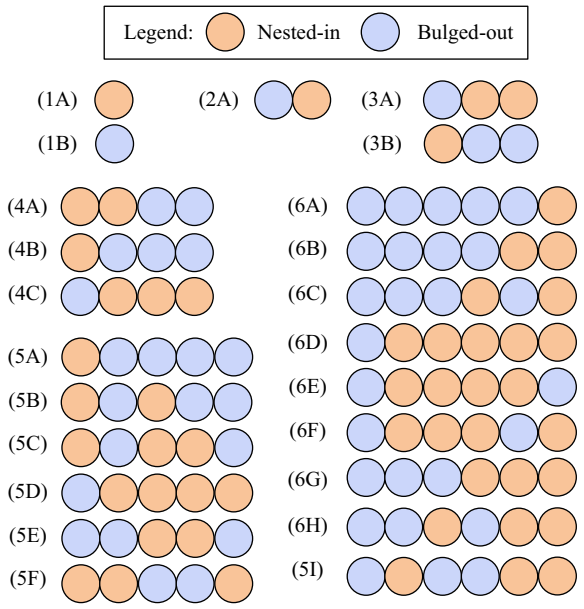

FIG. 5. All possible layouts of the periodic repeating cell consisting of 1, 2, 3, 4, 5, or 6 SMO units. By removing the duplicate cases, 23 cases are possible.

cell consists of 1 to 6 units along the height direction. If the cell consists of only one SMO unit, two layouts are possible, namely (1A) "0" and (1B) "1." If there are two units in a cell, at a first glance it appears that there are $2^2 = 4$ possible layouts which are "0-0," "1-1," "1-0," and "0-1," but this will reduce to two if we consider the repeatability with the one-unit situation [i.e., "0-0" and "1-1" are identical with layouts (1A) and (1B)]. By further accounting for the reflectional symmetry, layouts "1-0" and "0-1" are identical; hence, only one layout is left, i.e., (2A) "0-1." If the cell is made up of more than 2 cells, by overall considering the reflectional symmetry, the rotational symmetry, and the repeatability with the previous situations, then we can get the possible layouts without redundancy. For example, if we consider the cell with 3 units, then there are $2^3 = 8$ layouts at first, which can be reduced to 2 by considering the repeatability and the equivalence due to symmetry. In sum, for all the situations that the cell consists of 1 to 6 units, 23 different layouts are possible, as illustrated in Fig. 5.

B. Wave propagation along the height direction

With the 23 possible layouts of the periodic repeating cell, we then investigate the achievable frequency band that the wave propagation is prohibited. To this end, based on the same driving amplitude, viscous damping coefficient, and initial conditions as those used in Fig. 4, numerical frequency sweeps are performed from 5 to 75 Hz. Figure 6 shows the transmissibility and the corresponding stopbands (transmissibility lower than 0.1) of the 23 cases.

Figure 6 reveals two important characteristics that are unique for the SMO metastructure. First, with more SMO units in the periodic repeating cell, the stopband of the metastructure is substantially extended to the low-frequency region. For example, if the cell consists of only one cell, then two

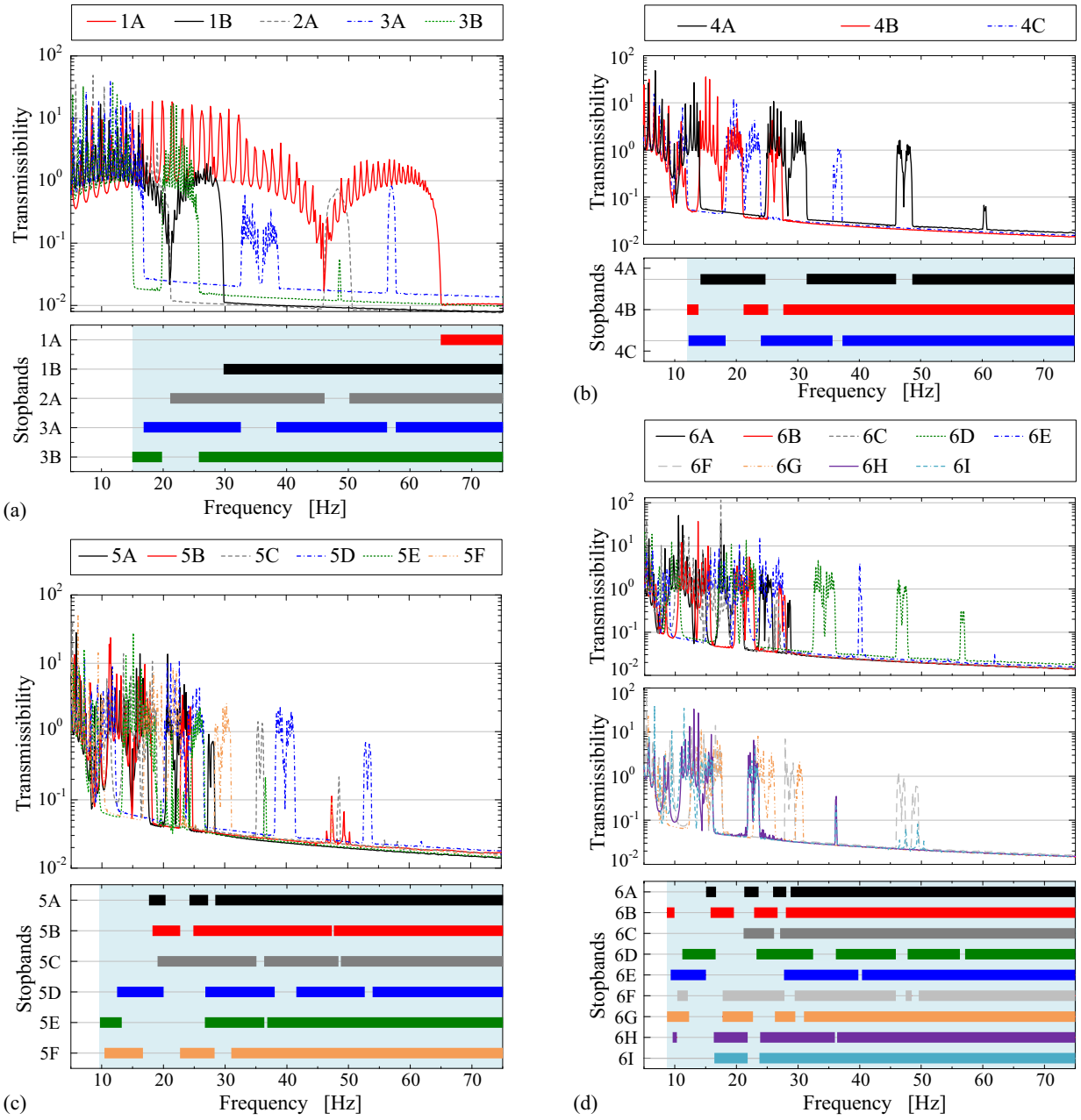

FIG. 6. Transmissibility and stopbands of the SMO metastructure corresponding to 23 different layouts of the periodic repeating cell configurations and their band structure. (a) Cases with layouts (1A), (1B), (2A), (3A), and (3B). (b) Cases with layouts (4A), (4B), and (4C). (c) Cases with layouts (5A), (5B), (5C), (5D), (5E), and (5F). (d) Cases with layouts (6A), (6B), (6C), (6D), (6E), (6F), (6G), (6H), and (6I).

layouts are possible, and the overall stopband (denoted by shades in the bottom panels) spans from 29.8Hz to infinity. By involving more units in a cell, the lower bound of the overall stopband would be extended downward significantly, from 21.2 Hz when the cell consists of two SMO units, to 15.0 Hz, to 12.2 Hz, to 9.7 Hz, and to 8.7 Hz when the cell consists of three, four, five, and six SMO units, respectively. Second, the capability of switching between two stable configurations and the rich layout possibilities of the periodic cell endow the SMO metastructure with excellent tunability and programmability of the stopband. Based on the 23 possible layouts, the achievable stopband would become $[8.7, \infty]$ Hz. Within this stopband, wave propagation at any prescribed frequency can always be prohibited by strategically tuning the number of the constituent SMO units in the periodic cell and coding the state sequence. For example, if we intend to prohibit the wave propagation at 20.0 Hz and the number of SMO units in a periodic cell is asked to be no more than 4, by referring to Fig. 6, we realize that effective prohibition can be achieved in two cases, namely, (3A) and (4A). Hence, by adjusting the state sequence of the periodic cell into (3A) "1-0-0" or (4A) "0-0-1-1," the wave can no longer be propagated through the metastructure. Note that if allowing more units in a cell, more possibilities can be found. Figure 6 also suggests that if aiming at prohibition at relatively higher frequencies, we would have more choices of the cell layouts; however, if

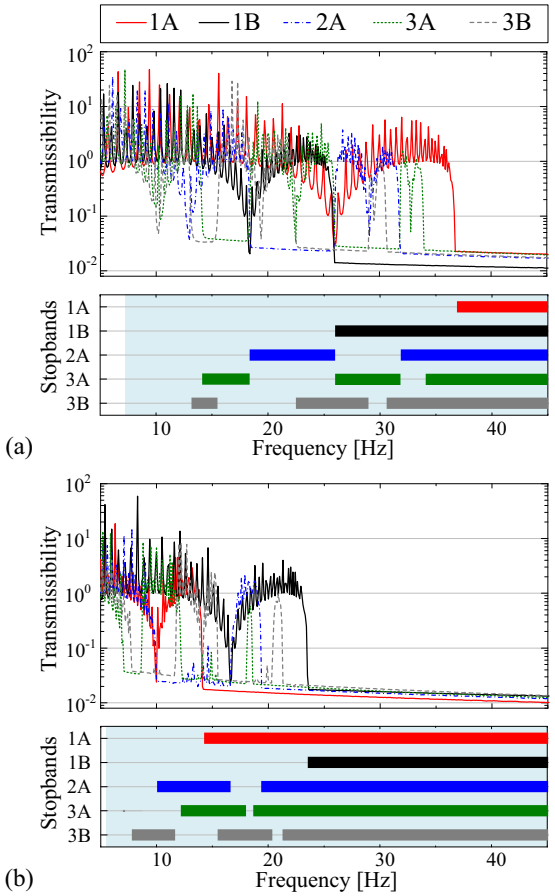

FIG. 7. Transmissibility and stopbands of the SMO metastructure corresponding to five different layouts along the length and the width directions. (a) Cases with layouts (1A), (1B), (2A), (3A), and (3B) along the length direction. (b) Cases with layouts (1A), (1B), (2A), (3A), and (3B) along the width direction.

looking for prohibition near the lower frequency bound, then the layout choices become limited.

C. Wave propagation along the width and the length directions

Note that the origami unit is a true 3D structure, which is fundamentally different from many conventional 1D and 2D units constituting metamaterials and metastructures [26]. As a result, it is necessary and interesting to examine the wave propagation characteristics of the SMO metastructure along the other two principal directions, i.e., the length and the width directions. This would make more sense if we realize that the constitutive relations of the SMO unit are very anisotropic along the three principal directions [Figs. 2(d)–2(f)]. To this end, assuming that the metastructure is constructed by connecting the SMO units along the length or the width direction, systematic numerical studies are carried out based on the same setup. Similarly, 23 possible layouts of the periodic cell are examined. As examples, Figs. 7(a) and 7(b) display the transmissibility and stopbands of the metastructure with layouts (1A), (1B), (2A), (3A), and (3B) along the length and the width directions, respectively. For reference purposes, based on 23 possible layouts, the overall achievable stopbands along the width and the length directions are also denoted by shades

TABLE II. Design parameters of SMO unit "2" in the counterexample.

Parameters	Values	Parameters	Values
$b_A = b_B = b$	38.1 mm	γ_A	60°
a_A	38.1 mm	γ_B	75°
$k_A = k_C$	0.05 N	k_B	2 N

(bottom panels). Figure 7 reveals that along the length direction, the achievable stopband spans from 7.1 Hz to infinity, and along the width direction, the achievable stopband spans from 5.5 Hz to infinity. Note that the lower-frequency bounds of the stopbands along the width and length directions are much lower than that along the height direction; meanwhile, for a specific periodic cell layout, the overall band structures along the three directions show considerable differences. Such discrepancies are induced by the anisotropy of the constitutive relations, particularly, the different tangent stiffness at the stable configuration along the three principal directions.

The above observation also suggests that the excellent tunability and programmability of the SMO metastructure are preserved along the length and width directions. Prohibiting the wave propagation at any frequency within the achievable stopband can be realized by coding the status sequence of the periodic cell.

It is also worth pointing out here that a broad and programmable stopband is not always achievable. Rather, they rely on appropriate geometry and mechanical parameters of the SMO unit. Here, we demonstrate a counterexample to illustrate this point. In this example, the design parameters of the SMO unit are listed in Table II. For distinction purposes, in what follows, the SMO unit with parameters listed in Table II is referred as SMO unit "2," and the SMO unit with parameters listed in Table I is referred as SMO unit "1." Based on SMO unit "2," similar numerical frequency sweeps are performed on the SMO metastructure along the three principal directions, and Figs. 8(d)–8(f) show the corresponding transmissibility and stopbands with layouts (1A), (1B), (2A), (3A), and (3B). Figures 8(d)–8(f) indicate that along the height and the width directions, the stopbands would experience significant changes when adjusting the layout of the periodic cell. More specifically, based on SMO unit "1," with five layouts (i.e., 1A, 1B, 2A, 3A, and 3B), the achievable stopband along the width direction already fully cover the frequency interval [5.5, 45.0] Hz (Fig. 7); rather, for the counterexample based on SMO unit "2," there are still some frequency intervals, such as [10.7, 11.2] Hz and [12.3, 13.8] Hz, cannot be covered by the stopband. The situation along the length direction is even deteriorated. Unlike the case based on SMO unit "1" (Fig. 7), for SMO unit "2," changing the layout of the periodic cell has little effect on the stopband. These observations indicate that the stopband tunability and programmability of this metastructure are weakened along the width direction, and may completely vanish along the length direction.

Note that with small excitation amplitude, the tangent stiffness at the stable configurations play a dominant role in determining the stopband of the metastructure [43]. Thus,

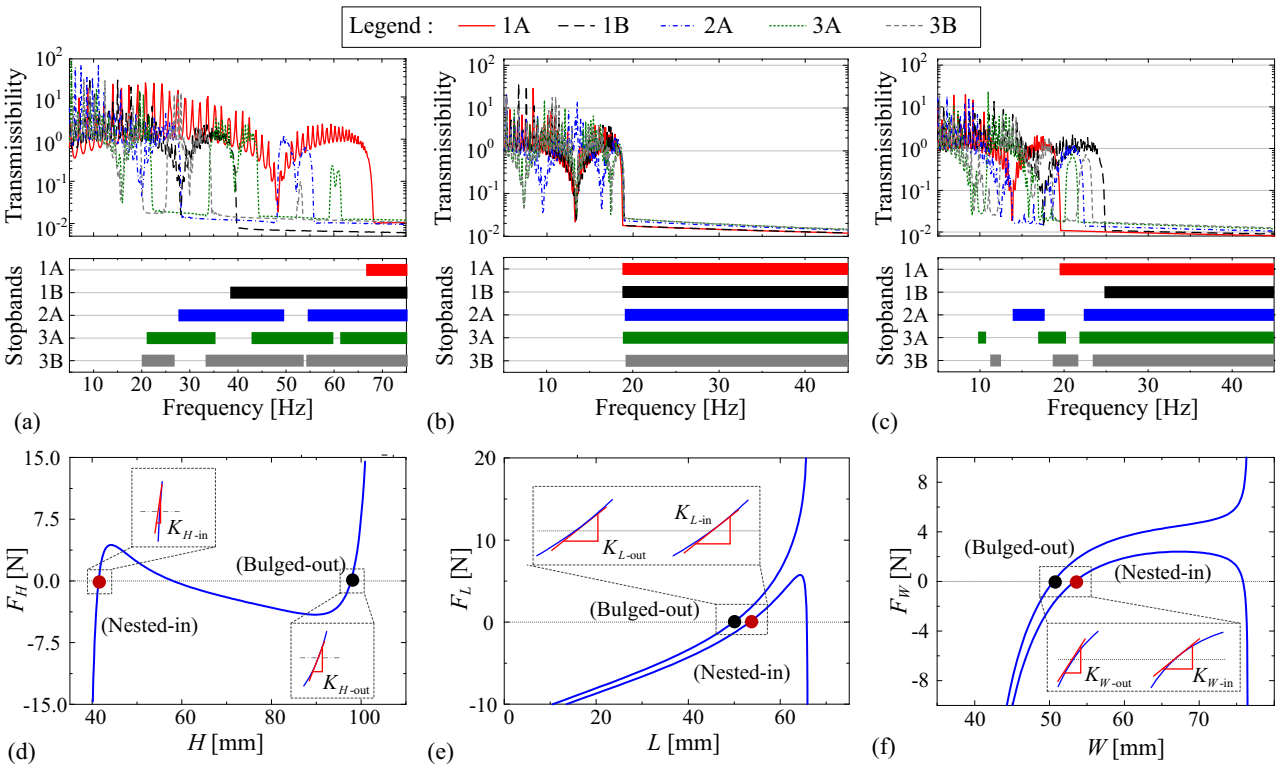

FIG. 8. The transmissibility, stopbands, and force-displacement curve of the SMO metastructure corresponding to 5 layouts along three principal directions based on SMO unit "2" (with design parameters listed in Table II). Panels (a)–(c) show the transmissibility and stopbands of the SMO metastructure along the height, the length, and the width directions, respectively. Along each direction, five layouts are examined, namely, (1A), (1B), (2A), (3A), and (3B). Panels (d)–(f) display the force-displacement curves along the height, the length, and the width directions, respectively.

the above worsening or even deterioration of the stopband tunability and programmability can be interpreted in terms of the tangent stiffness at the stable configurations. To this end, for SMO unit "2," the force-displacement relations along the height, length, and width directions are displayed in Figs. 8(a)–8(c), respectively. For both SMO units, the tangent stiffness at the nested-in and the bulged-out configurations along the three principal directions are calculated and listed in Table III. Table III reveals clearly that for both SMO units, along the height direction, the tangent stiffness difference is significant ($\Delta K_H = 3.2$N/mm and 3.3N/mm corresponding to SMO units "1" and "2," respectively), which accounts for the good tunability and programmability of the stopband along the height direction. Along the width direction, the stiffness difference for both units are substantially decreased, and SMO unit "1" outstrips SMO unit "2" ($\Delta K_W = 0.48$N/mm and 0.31N/mm corresponding to SMO units "1" and "2," respectively), explaining why SMO unit "1" could induce better stopband tunability and programmability. Along the length direction, for SMO unit "2," the stiffness difference completely vanishes ($\Delta K_L \approx 0$). This explains why along the length direction the stopbands are almost the same for different layouts of the periodic cell. Figure 8 and Table III also provide useful hints for designing metastructures. To acquire programmability along all three principal directions, the constituent cell should be designed such that along each direction, the tangent stiffness at the two stable configurations are significantly different.

TABLE III. Tangent stiffness of the SMO units along the three principal directions.

	SMO unit "1" with parameters listed in Table I			SMO unit "2" with parameters listed in Table II	
	Tangent stiffness	Stiffness difference		Tangent stiffness	Stiffness difference
Height direction	$K_{H-\text{in}} = 4.5$ N/mm $K_{H-\text{out}} = 1.2$ N/mm	$\Delta K_H = 3.3$ N/mm	Height direction	$K_{H-\text{in}} = 5.1$ N/mm $K_{H-\text{out}} = 1.9$ N/mm	$\Delta K_H = 3.2$ N/mm
Width direction	$K_{W-\text{in}} = 0.23$ N/mm $K_{W-\text{out}} = 0.71$ N/mm	$\Delta K_W = 0.48$ N/mm	Width direction	$K_{W-\text{in}} = 0.45$ N/mm $K_{W-\text{out}} = 0.76$ N/mm	$\Delta K_W = 0.31$ N/mm
Length direction	$K_{L-\text{in}} = 1.7$ N/mm $K_{L-\text{out}} = 0.72$ N/mm	$\Delta K_L = 0.98$ N/mm	Length direction	$K_{L-\text{in}} = 0.42$ N/mm $K_{L-\text{out}} = 0.42$ N/mm	$\Delta K_L \approx 0$

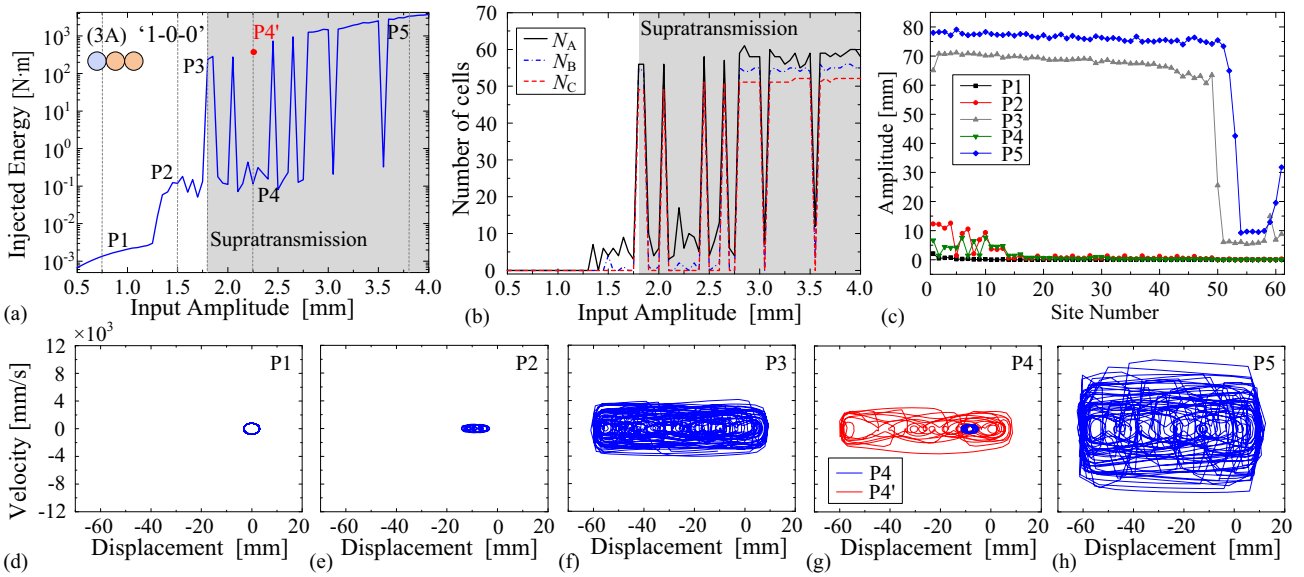

FIG. 9. Supratransmission phenomenon of the SMO metastructure based on layout (3A). (a) The injected energy as a function of the input amplitude in the logarithmic scale. (b) Three indicators N_A, N_B, and N_C with respect to the input amplitude. (c) Amplitudes of the 61 SMO units at five different input amplitudes. (d)–(h) Phase diagrams of the first SMO unit at five input amplitudes.

V. SUPRATRANSMISSION: THRESHOLD VALUE AND MECHANISM ANALYSIS

Note that the above stopband analyses are carried out based on the assumption that the excitation amplitude is small. We are then interested to know the behavior of the metastructure with the increase of the excitation amplitude when the input frequency locates inside the stopband.

Here, we revisit the metastructure composed of 60 SMO units that are connected along the height direction. The design parameters of the SMO unit are given in Table I. As an example, the periodic repeating cell layout (3A) "1-0-0" is examined first. To minimize the wave reflection effect and to mimic an infinite medium, viscous damping (with damping ratio 0.15) is assumed in the last 10 oscillators to simulate an absorbing boundary. The initial displacement and initial velocity are assumed to be zero for all oscillators. Here, displacement excitation is applied to the mass of the first oscillator (#0) next to the left boundary. The excitation frequency is prescribed to be 40 Hz, which locates inside the stopband; the excitation amplitude is increased from 0.5 to 4.0 mm, with step 0.05 mm. The simulation time is set as 20 000 times of the excitation period (i.e., 500 s) to reach the steady state.

To examine the overall behavior of the metastructure, the injected energy is selected as an index to evaluate the energy transmission. Specifically, the energy injected into the metastructure by the driving boundary over the simulation time is can be expressed as [33]

$$E_{\text{in}} = \int_0^{nT} F(z_1 - z_{\text{input}})\dot{z}_{\text{input}}\,dt, \tag{15}$$

where F represents the force-displacement relations of the first SMO unit; it can be either F_{in} or F_{out}, depending on whether the first unit is at the nested-in or at the bulged-out configuration. For the layout (3A) "1-0-0," F takes F_{out}. T is the period of the excitation, and n takes 20 000 in our simulations. We also define three indicators, namely, N_A, N_B, and N_C, to quantify the behaviors of the SMA units (or, the oscillators). In detail, N_A quantifies the number of oscillators that experience at least one snap-through transition from one stable configuration to the other during the whole simulation time; N_B quantifies the number of oscillators that no longer stay at the initial stable configuration (in another word, stay at the other stable configuration) when the simulation ends; N_C quantifies the number of oscillators that undergo interwell oscillations (which is a large amplitude oscillation surrounding both stable equilibria [15]) during the steady state (last at least 5000 periods).

Figure 9(a) displays the relationship between the injected energy and the input amplitude, in logarithmic scale, and Fig. 9(b) plots the three indicators with respect to the input amplitude. When the input amplitude is relatively small, only little energy can be transmitted through the metastructure since the input frequency locates inside the stopband. For example, with amplitude 0.75 mm (point P1 in Fig. 9), the injected energy is of order $O(10^{-3})$, and all the three indicators equal to 0. We also plot the phase diagram of the first SMO unit (#1) at this excitation [Fig. 9(d)], which indicates that the SMO unit is executing an intrawell oscillation around the bulged-out stable configuration. With a small amplitude of the first oscillator and low injected energy, the vibration can hardly propagate beyond the second oscillator, which can be observed from the amplitudes of all oscillators shown in Fig. 9(c). By increasing the input amplitude to 1.25 mm, the injected energy gradually increases; however, all three indicators remain zero, indicating that no qualitative change occurs on the dynamics of the metastructure. When the input amplitude is larger than 1.25 mm, a small jump of the injected energy is witnessed, accompanied by a small increase of N_A. To understand the underlying reason, point P2 with input amplitude 1.5 mm is studied. The phase diagram [Fig. 9(e)] indicates that the first SMO unit still performs an intrawell

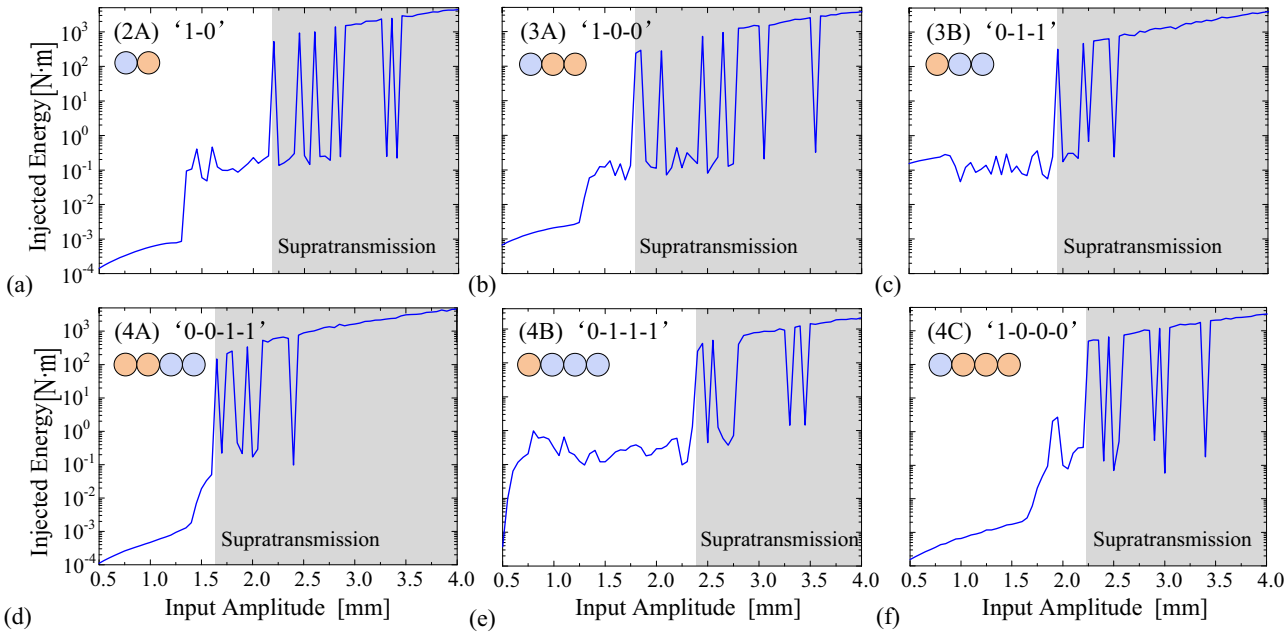

FIG. 10. The relationships between the injected energy and the input amplitude corresponding to six layouts. (a) layout (2A), (b) layout (3A), (c) layout (3B), (d) layout (4A), (e) layout (4B), and (f) layout (4C). The shaded regions represent the input amplitudes that can trigger supratransmission.

oscillation but with larger amplitude, which was described as resonant intrawell oscillation [15]. This explains why the inject energy reaches the order of $O(10^{-1})$, N_A and N_B becomes positive, and the vibration could propagate to the 13th oscillator [Fig. 9(c)]. Keep increasing the amplitude, both the injected energy and the indicators N_A, N_B, and N_C experiences upsurges at 1.8 mm (point P3). In detail, the injected energy elevates to the order of $O(10^2)$, N_A and N_B are above 55, and N_C is close to 50. Such significant rises are induced by the transition from small-amplitude intrawell oscillations to large-amplitude interwell oscillations, as is depicted in the phase diagram shown in Fig. 9(f). The large amplitude vibration can also propagate until the 49th oscillators [Fig. 9(c)]. Actually, it is the interwell oscillation that triggers the supratransmission phenomena, and the amplitude at point P3 (i.e., 1.8 mm) is the threshold value for supratransmission. Before the threshold, the injected energy is spatially attenuated away from the input and does not propagate along the chain; when exceeding the threshold, even though the frequency locates within the stopband, energy transmission becomes possible due to the nonlinear instability induced interwell oscillations.

It is worthwhile pointing out here that if the input amplitude is above the threshold (shaded area), the occurrence of supratransmission also depends on the initial conditions of the constituent oscillators of the metastructure. This is because the SMO unit is fundamentally a bistable system, whose behavior is sensitive to initial conditions. For example, at point P4 with amplitude 2.25 mm, supratransmission does not happen. The injected energy as well as the indicators N_A, N_B, and N_C fall back to the levels similar to those corresponding to point B. This is because, at this amplitude and initial conditions, the first oscillator performs a small-amplitude intrawell oscillation [Fig. 9(g)], while the instability-induced interwell oscillation is not activated. As a result, the vibration propagation stops at the 13th oscillator. However, if we change the initial velocity of the first unit in each periodic cell to -800 mm/s [point P' in Fig. 9(b)], supratransmission is regained, with the injected energy returning to the order of $O(10^2)$. This is also manifested by the phase diagram of the first unit (#1), which is an obvious large-amplitude interwell oscillation [Fig. 9(g)]. At another point P5 with amplitude 3.8mm, supratransmission phenomenon is observed again. Both the injected energy and the indicators N_A, N_B, and N_C take large values. The first oscillator undergoes a large-amplitude interwell oscillation [Fig. 9(h)], and the vibration is able to propagate to the 52nd oscillator [Fig. 9(c)].

Note that the layout of the periodic repeating cell could significantly affect the number and location of the stopbands. We then investigate the effects of the layouts on the threshold amplitude of supratransmission. In detail, based on the same setup, numerical amplitude sweeps are carried out on the SMO metastructure. Six layouts of the periodic cell, namely, (2A), (3A), (3B), (4A), (4B), and (4C), are examined. Figure 10 illustrates the relationships between the injected energy and the input amplitude in the logarithmic scale corresponding to the six layouts. It shows that supratransmission always happens when increasing the input amplitude. However, the amplitude threshold varies significantly. In detail, corresponding to the six layouts, the threshold values are 2.20 mm for layout (2A), 1.80 mm for layout (3A), 1.95 mm for layout (3B), 1.65 mm for layout (4A), 2.40 mm for layout (4B), and 2.25 mm for layout (4C), respectively. Above the threshold (shaded areas), supratransmission is possible, but still sensitively depends on the initial conditions.

However, along the length and the width directions, although prominent stopbands are observed when the input amplitude is small, supratransmission phenomenon cannot occur by increasing the driving amplitude. This is because

the occurrence of supratransmission relies on the instability-induced high-energy response (for the bistable SMO unit, the large-amplitude interwell oscillation). However, along the width and the length directions, the constitutive relations are fundamentally different from that along the height direction. Particularly, the stable equilibria of the SMO unit stay on the same side of the unstable equilibrium [Figs. 2(b), 2(c), and 2(e), 2(f)], indicating that deforming along the width and the length directions cannot achieve a switch between the two stable configurations. As a result, along the length and the width directions, no matter how large the driving amplitude is, interwell oscillation of the SMO unit cannot be generated, and supratransmission phenomenon cannot be achieved.

VI. SUMMARY AND CONCLUSIONS

Owing to the infinite design possibilities and unique shape reconfigurability, origami, fundamentally the art of paper folding, receives extensive attention in developing metamaterials and metastructures. While rich outcomes have been achieved in the field of kinematics and statics, the dynamic characteristics of origami metamaterials and metastructures are less focused. Actually, we cannot ignore the necessity that origami structures have to work in dynamic environment or serves as a medium for wave propagation. Aiming at deepening our understanding of origami wave dynamics, this paper investigates the wave propagation characteristics of an origami metastructure composed of stacked Miura-origami (SMO) units. Originating from the nonunique geometry correspondence, the SMO unit has two topologically different stable configurations, namely, the nested-in and the bulged-out configurations. Through linear dispersion analyses and numerical calculations, we find that along the height direction, the SMO metastructure would prohibit wave propagation in some frequency intervals (i.e., stopbands) when the driving amplitude is small. Based upon that, by adjusting the layout of the periodic repeating cell, including the number and configurations of the SMO units, the stopbands would experience substantially changes. By utilizing this property, the bandgaps of the SMO metastructure can be effectively tailored. Moreover, by digitizing the two stable configurations into "0" and "1," the state sequence of the periodic cell can be strategically coded, we can then effectively program or tune the band structure toward requirements. We show that if the metastructure consists of 60 SMO units, 23 periodic cell layouts are possible; based on which, the stopband can be programmed within a broad frequency interval.

As the input amplitude increases, we find that the energy propagating through the metastructure could experience a sudden jump, even though the driving frequency locates within the stopband. Such supratransmission phenomenon and the threshold amplitude are evaluated by the injected energy and three indexes describing the number of units relating to the snap-through transitions. We demonstrate that the supratransmission is triggered by the occurrence of large amplitude inter-well oscillation of the constituent cell, which is a characteristic behavior of the system with bistability or instability. It is also revealed that the occurrence of supratransmission phenomenon also relies on initial conditions, because the bistability is a strong nonlinearity, and the trigger—interwell oscillation—sensitively depend on the initial conditions. Moreover, through some examples, we show that the threshold amplitude of supratransmission is also tailorable by adjusting the periodic cell layouts.

We also remark in this paper that by tessellating the SMO units along different directions, we can construct different metastructures based on the same constituent units. The above wave propagation studies are then extended to the other two directions. Overall, due to the anisotropy in constitutive relations, the band structures along the three principal directions are significantly different. Numerical results confirm the stopband tunability and programmability along the length and the width directions. However, these features could disappear if the design parameters are not appropriately prescribed. However, since the SMO unit cannot switch its configuration by changing the unit's length or width, supratransmission of energy cannot be observed along the length or the width direction. It is also worth pointing out here that although the band structures along all the three directions are considered, they are examined independently, i.e., the interactions from the other two directions are not considered. This brings up several interesting questions that are worthy of future study, i.e., How does the wave propagate when the metastructure is constructed by tessellating the origami units along all the three directions? How do the interactions among the three directions affect the programmability and tunability of the dynamics?

This research performs a comprehensive investigation on the wave dynamics of an SMO metastructure. By uncovering the unique stopband tunability and programmability as well as the underlying mechanism of the supratransmission phenomenon, the present work could significantly advance the state of the art and open new perspectives for origami dynamics research. The results also lay a solid foundation for developing origami-based metamaterials and metastructure with adaptive dynamic properties.

ACKNOWLEDGMENTS

This research was supported by the National Natural Science Foundation of China under Awards No. 11902078 and No. 11932015, and the Major Research Plan of the National Natural Science Foundation of China under Grant No. 91748203.

[1] J. A. Faber, A. F. Arrieta, and A. R. Studart, Science **359**, 1386 (2018).

[2] S. Guitron, A. Guha, S. Li, and D. Rus, in *Proceedings of the IEEE International Conference on Robotics and Automation (ICRA)* (IEEE, Piscataway, NJ, 2017), pp. 4807–4813.

[3] S. Li, H. Fang, S. Sadeghi, P. Bhovad, and K. W. Wang, Adv. Mater. **31**, 1805282 (2019).

[4] M. Schenk and S. D. Guest, Proc. Natl. Acad. Sci. USA **110**, 3276 (2013).

[5] S. Li and K. W. Wang, J. R. Soc., Interface **12**, 20150639 (2015).

[6] H. Yasuda and J. Yang, Phys. Rev. Lett. **114**, 185502 (2015).

[7] H. Fang, T. Chang, and K.-W. Wang, Smart Mater. Struct. **29**, 015026 (2020).

[8] E. T. Filipov, T. Tachi, and G. H. Paulino, Proc. Natl. Acad. Sci. USA **112**, 12321 (2015).

[9] H. Fang, S.-C. A. Chu, Y. Xia, and K. W. Wang, Adv. Mater. **30**, 1706311 (2018).

[10] M. B. Pinson, M. Stern, A. C. Ferrero, T. A. Witten, E. Chen, and A. Murugan, Nat. Commun. **8**, 15477 (2017).

[11] J. T. B. Overvelde, T. A. De Jong, Y. Shevchenko, S. A. Becerra, G. M. Whitesides, J. C. Weaver, C. Hoberman, and K. Bertoldi, Nat. Commun. **7**, 10929 (2016).

[12] H. Fang, S. Li, and K. W. Wang, Proc. R. Soc. London, Ser. A **472**, 20160682 (2016).

[13] H. Fang, K. W. Wang, and S. Li, Extreme Mech. Lett. **17**, 7 (2017).

[14] S. Li, H. Fang, and K. W. Wang, Phys. Rev. Lett. **117**, 114301 (2016).

[15] H. Fang, S. Li, H. Ji, and K. W. Wang, Phys. Rev. E **95**, 052211 (2017).

[16] H. Yasuda, C. Chong, E. G. Charalampidis, P. G. Kevrekidis, and J. Yang, Phys. Rev. E **93**, 043004 (2016).

[17] H. Yasuda, Y. Miyazawa, E. G. Charalampidis, C. Chong, P. G. Kevrekidis, and J. Yang, Sci. Adv. **5**, eaau2835 (2019).

[18] M. Thota, S. Li, and K. W. Wang, in *Proceedings of the ASME 2016 Conference on Smart Materials, Adaptive Structures and Intelligent Systems* (American Society of Mechanical Engineers Digital Collection, New York, NY, 2016).

[19] M. Thota, S. Li, and K. W. Wang, Phys. Rev. B **95**, 064307 (2017).

[20] M. Thota and K. W. Wang, J. Appl. Phys. **122**, 154901 (2017).

[21] J. Meaud and K. Che, Int. J. Solids Struct. **122**, 69 (2017).

[22] G. Wang, D. Yu, J. Wen, Y. Liu, and X. Wen, Phys. Lett. A **327**, 512 (2004).

[23] S. Krödel, N. Thomé, and C. Daraio, Extreme Mech. Lett. **4**, 111 (2015).

[24] M. S. Kushwaha, P. Halevi, L. Dobrzynski, and B. Djafari-Rouhani, Phys. Rev. Lett. **71**, 2022 (1993).

[25] E. Yablonovitch, Phys. Rev. Lett. **58**, 2059 (1987).

[26] Z. Wu, Y. Zheng, and K. W. Wang, Phys. Rev. E **97**, 022209 (2018).

[27] Z.-Y. Li and L.-L. Lin, Phys. Rev. E **67**, 046607 (2003).

[28] I. V. Shadrivov, A. A. Sukhorukov, and Y. S. Kivshar, Phys. Rev. Lett. **95**, 193903 (2005).

[29] J. O. Vasseur, P. A. Deymier, A. Khelif, P. Lambin, B. Djafari-Rouhani, A. Akjouj, L. Dobrzynski, N. Fettouhi, and J. Zemmouri, Phys. Rev. E **65**, 056608 (2002).

[30] Y. Pennec, B. Djafari-Rouhani, J. O. Vasseur, A. Khelif, and P. A. Deymier, Phys. Rev. E **69**, 046608 (2004).

[31] I. E. Psarobas and M. M. Sigalas, Phys. Rev. B **66**, 052302 (2002).

[32] B. R. Mace and E. Manconi, J. Sound Vib. **318**, 884 (2008).

[33] F. Geniet and J. Leon, Phys. Rev. Lett. **89**, 134102 (2002).

[34] J. E. Macías-Díaz and A. Bountis, Commun. Nonlinear Sci. Numer. Simul. **63**, 307 (2018).

[35] J. E. Macías-Díaz, Phys. Rev. E **77**, 016602 (2008).

[36] P. Anghel-Vasilescu, J. Dorignac, F. Geniet, J. Leon, and M. Taki, Phys. Rev. Lett. **105**, 074101 (2010).

[37] H. Susanto and N. Karjanto, J. Nonlin. Optic. Phys. Materials **17**, 159 (2008).

[38] A. B. T. Motcheyo, J. D. T. Tchameu, M. S. Siewe, and C. Tchawoua, Commun. Nonlin. Sci. Numer. Simul. **50**, 29 (2017).

[39] A. B. T. Motcheyo, C. Tchawoua, M. S. Siewe, and J. D. T. Tchameu, Commun. Nonlin. Sci. Numer. Simul. **18**, 946 (2013).

[40] R. Khomeriki, S. Lepri, and S. Ruffo, Phys. Rev. E **70**, 066626 (2004).

[41] M. J. Frazier and D. M. Kochmann, J. Sound Vib. **388**, 315 (2017).

[42] Y. Zheng, Z. Wu, X. Zhang, and K. W. Wang, Smart Mater. Struct. **28**, 45005 (2019).

[43] Z. Wu and K. W. Wang, J. Sound Vib. **458**, 389 (2019).

[44] S. Sengupta and S. Li, J. Intell. Mater. Syst. Struct. **29**, 2933 (2018).